Check for updates

ADVANCED MATERIALS
www.advmat.de

Electrically Switchable Polarization in Bi_2O_2Se Ferroelectric Semiconductors

*Weijun Wang, You Meng, Yuxuan Zhang, Zhuomin Zhang, Wei Wang, Zhengxun Lai, Pengshan Xie, Dengji Li, Dong Chen, Quan Quan, Di Yin, Chuntai Liu, Zhengbao Yang, SenPo Yip, and Johnny C. Ho**

Atomically 2D layered ferroelectric semiconductors, in which the polarization switching process occurs within the channel material itself, offer a new material platform that can drive electronic components toward structural simplification and high-density integration. Here, a room-temperature 2D layered ferroelectric semiconductor, bismuth oxychalcogenides (Bi_2O_2Se), is investigated with a thickness down to 7.3 nm (≈12 layers) and piezoelectric coefficient (d_{33}) of 4.4 ± 0.1 pm V^{-1}. The random orientations and electrically dependent polarization of the dipoles in Bi_2O_2Se are separately uncovered owing to the structural symmetry-breaking at room temperature. Specifically, the interplay between ferroelectricity and semiconducting characteristics of Bi_2O_2Se is explored on device-level operation, revealing the hysteresis behavior and memory window (MW) formation. Leveraging the ferroelectric polarization originating from Bi_2O_2Se, the fabricated device exhibits "smart" photoresponse tunability and excellent electronic characteristics, e.g., a high on/off current ratio > 10^4 and a large MW to the sweeping range of 47% at V_{GS} = ±5 V. These results demonstrate the synergistic combination of ferroelectricity with semiconducting characteristics in Bi_2O_2Se, laying the foundation for integrating sensing, logic, and memory functions into a single material system that can overcome the bottlenecks in von Neumann architecture.

1. Introduction

Driven by the unprecedented explosion of a data-centric era, high-integrity ferroelectric electronic components are considered at the forefront of semiconductor electronics to satisfy emerging functional diversifications, e.g., nonvolatile memory, logic, artificial brain, neuromorphic sensors, etc.[1] However, most ferroelectrics, such as perovskites[2] or polyvinylidene fluoride,[3] are wide-bandgap insulators with poor electron mobility, which are challenging for rich functionalities.[4] Although the device concept based on semiconductor/ferroelectric heterostructures provides an alternate choice, the polarization switching process of the device configuration occurs within the ferroelectric dielectrics, intrinsically unfavorable for device simplification,[5] interfacial issues reduction,[6] and channel controllability.[7] Besides, dielectric/ferroelectric instability or disappearance exists in the ferroelectrics below a critical thickness,[8] impeding their industrial miniaturization toward fundamental physical limits. In these regards, 2D layered ferroelectric semiconductors are appealing, in which polarization switching occurs within the channel material itself, offering a new material platform that could drive electronic components toward simplification and miniaturization.[9]

Except for the synergistic combination of ferroelectricity with semiconducting characteristics, the 2D layered ferroelectric semiconductors also possess many other intriguing

W. Wang, Y. Meng, Y. Zhang, W. Wang, Z. Lai, P. Xie, D. Li, D. Chen, Q. Quan, D. Yin
Department of Materials Science and Engineering
City University of Hong Kong
Kowloon, Hong Kong SAR 999077, P. R. China

Z. Zhang, Z. Yang
Department of Mechanical Engineering
City University of Hong Kong
Kowloon, Hong Kong SAR 999077, P. R. China

C. Liu
Key Laboratory of Advanced Materials Processing & Mold
(Zhengzhou University)
Ministry of Education
Zhengzhou 450002, P. R. China

S. Yip, J. C. Ho
Institute for Materials Chemistry and Engineering
Kyushu University
Fukuoka 816-8580, Japan
E-mail: johnnyho@cityu.edu.hk

J. C. Ho
State Key Laboratory of Terahertz and Millimeter Waves
City University of Hong Kong
Kowloon, Hong Kong SAR 999077, P. R. China

J. C. Ho
Hong Kong Institute for Advanced Study
City University of Hong Kong
Kowloon, Hong Kong SAR 999077, P. R. China

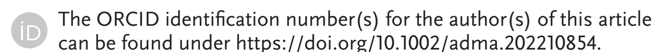
The ORCID identification number(s) for the author(s) of this article can be found under https://doi.org/10.1002/adma.202210854.

DOI: 10.1002/adma.202210854

 © 2023 Wiley-VCH GmbH

features, e.g., ultrathin geometry, absence of dangling bonds, and easy integration.[7] Despite the potential importance of 2D layered ferroelectric semiconductors, only a few examples, e.g., In_2Se_3,[10] $MoTe_2$,[8b] WTe_2,[11] and SnS,[12] have been experimentally discovered thus far. Intriguingly, semiconducting Bi_2O_2Se has been discovered with room-temperature ferroelectricity due to the broken inversion symmetry induced by spontaneous lattice distortion.[13] Moreover, air-stable Bi_2O_2Se possesses almost all attractive semiconducting properties at the atomic limit, e.g., moderate bandgap (bulk ≈0.8 eV), high carrier mobility (up to 410 $cm^2 V^{-1} s^{-1}$), and unprecedented optical sensitivity.[14] However, fulfilling the potential of ferroelectric semiconductors in functional electronics requires achieving the interplay between ferroelectricity and semiconducting characteristics on the device-level operation, which is currently lacking since the research on ferroelectricity of Bi_2O_2Se is still in its infancy.[13,15]

Herein, we systematically investigated the ferroelectricity and electronic characteristics of the ultrathin Bi_2O_2Se flakes synthesized by the chemical vapor deposition (CVD) method. Using the piezoresponse force microscopy (PFM), the out-of-plane (OOP) ferroelectric polarization of the ultrathin Bi_2O_2Se with a thickness down to 7.3 nm was investigated. A systematic theoretical analysis, combining ab initio molecular dynamics (AIMD) simulation with density functional theory (DFT) calculation, is performed to gain deep insight into its ferroelectric origin and electrically ferroelectric polarization switching. The device-level interplay between ferroelectricity and electronic characteristics based on the 2D Bi_2O_2Se ferroelectric semiconductor field-effect transistors (FeS-FETs) was investigated. Moreover, a unique ferroelectric semiconductor photodetector (FeS-PD) with nonvolatile functionality and controllability is developed owing to the reproducibly remnant polarization switching in ferroelectric semiconductors.

2. Results and Discussion

2.1. Characterizations of CVD-Grown Bi_2O_2Se Nanoflakes

Figure 1a shows 2D Bi_2O_2Se flakes with square or rectangular shapes synthesized by the CVD method. The atomic force

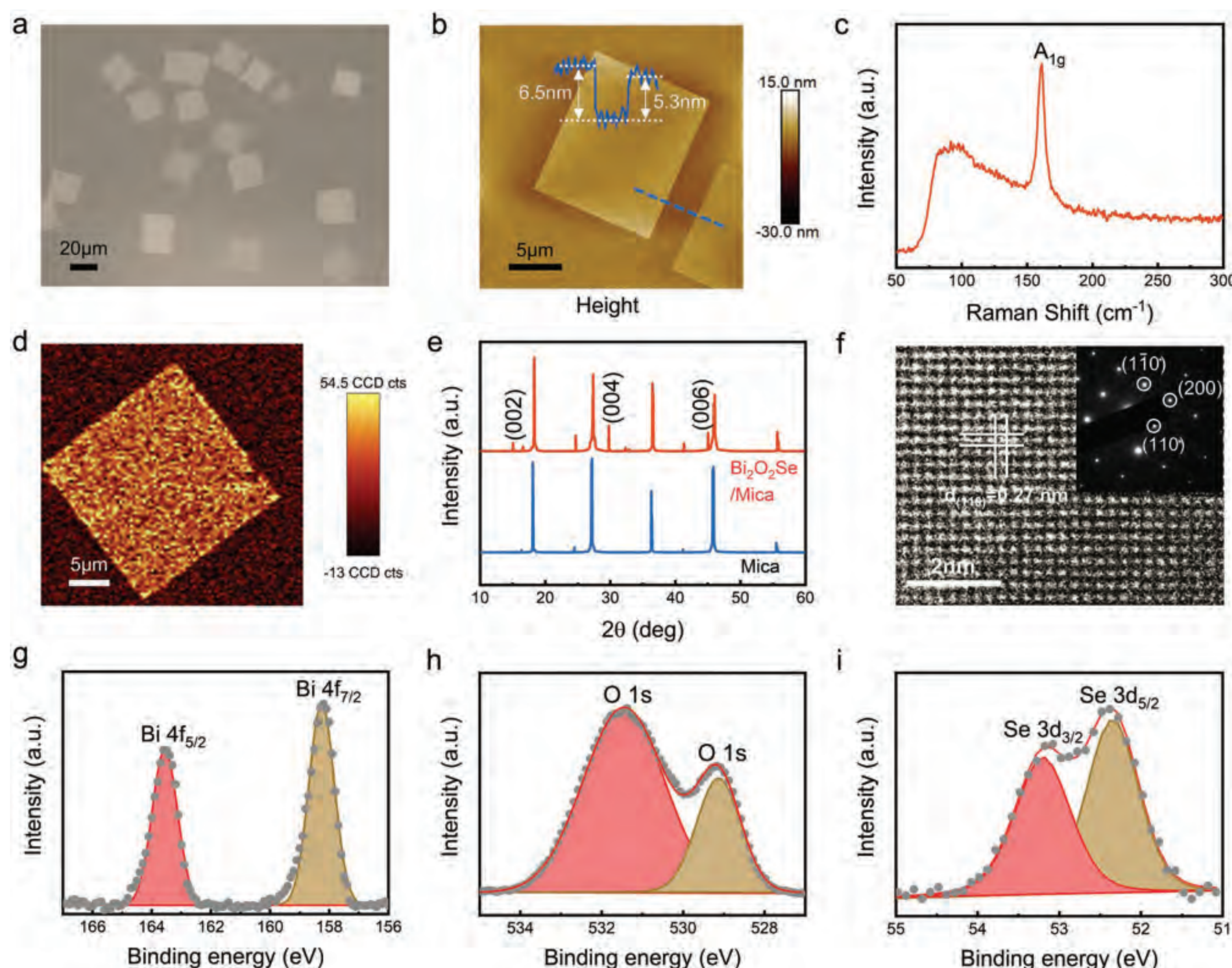

Figure 1. a) Optical image and b) AFM topography image of the CVD-grown Bi_2O_2Se flakes on mica. c) Raman spectrum and d) Raman mapping of the as-grown Bi_2O_2Se A_{1g} peak. e) XRD analysis of the pristine mica substrate and the Bi_2O_2Se flakes on mica. f) HRTEM image of Bi_2O_2Se flakes indicating the d-spacings of 2.74 Å for (110) planes. The inset SAED pattern of Bi_2O_2Se flakes shows its single crystallinity. g–i) XPS spectra and related fitting analysis of the as-grown Bi_2O_2Se flakes on mica.

 © 2023 Wiley-VCH GmbH

15214095, 2023, 12, Downloaded from https://onlinelibrary.wiley.com/doi/10.1002/adma.202210854 by City University Of Hong Kong, Wiley Online Library on [19/04/2023]. See the Terms and Conditions (https://onlinelibrary.wiley.com/terms-and-conditions) on Wiley Online Library for rules of use; OA articles are governed by the applicable Creative Commons License

microscope (AFM) test in Figure 1b shows that the thickness of as-grown Bi_2O_2Se on mica was ≈6.5 nm. The root-mean-square surface roughness of Bi_2O_2Se was calculated to be 4.9 Å, demonstrating its atomic-scale flatness. As shown in Figure S1 (Supporting Information), submillimeter Bi_2O_2Se flakes with a maximal size of ≈332 µm could be obtained, and the average thicknesses are determined to be ≈7.5 nm, indicating the great potential of Bi_2O_2Se in the large-area synthesis with good thickness uniformity. Figure 1c shows a single characteristic peak of 159 cm^{-1} attributed to the A_{1g} vibrational modes of Bi_2O_2Se flakes,[16] and the corresponding Raman mapping of the A_{1g} peak is depicted in Figure 1d. Figure 1e shows the X-ray diffraction (XRD) pattern of Bi_2O_2Se on mica with a reference pattern of the blank mica substrate. The lattice planes were indexed as (002), (004), and (006), matching well with a reference diffractogram of a single-phase tetragonal structure of Bi_2O_2Se (I4/mmm, a = 3.9 Å and c = 12.2 Å), exhibiting its pure phase nature.[17] The high-resolution transmission electron microscopy (HRTEM) image of 2D Bi_2O_2Se indicated d-spacings of 2.8 and 3.7 Å for (110) and (101) planes, respectively, and the inset selective area electron diffraction (SAED) pattern indicated the high-quality and single-crystallinity of Bi_2O_2Se (Figure 1f). The X-ray photoelectron spectroscopy (XPS) spectrum was then performed to determine the chemical bonding states of Bi_2O_2Se flakes (Figure 1g,h), which is consistent with the previous report.[18] The overall characterizations clearly show that our CVD-grown Bi_2O_2Se flakes are of high quality.

2.2. Ferroelectricity and Piezoelectricity of Bi_2O_2Se Nanoflakes

As shown in **Figure 2**a (I,II), Bi_2O_2Se has a tetragonal anti-$ThCr_2Si_2$ structure[19] with an I_4/mmm space group symmetry (a = 3.9 Å, c = 12.2 Å).[20] The tetragonal Bi_2O_2Se structure is alternately stacked by positively charged $[Bi_2O_2]^{2+}$ and negatively charged Se^{2-} layers along the crystallographic c-direction. The relatively large tetragonal unit cell in the I_4/mmm space group is centrosymmetric.[14b] Surprisingly, the Bi_2O_2Se semiconductor exhibits excellent OOP ferroelectricity, owing to the structural symmetry-breaking easily induced by the strain, doping,[13a] or thickness reduction.[13b] Among them, fine structural distortion is the underlying cause that induces the ferroelectricity in Bi_2O_2Se, whose susceptibility to symmetry-breaking is similar to the behavior of lead halide perovskites.[21] Specifically, the electric field from ultrafast charge localization leads to the local ordering of fluctuating dipoles from unit cells and extended ordering of structural distortion and inversion symmetry break, producing spontaneous polarons in 2D Bi_2O_2Se.[15b] From the viewpoint of atomic configuration, the structure distortion of the large unit cell can be attributed to the displacements of atoms in the Se layers to the Bi_2O_2 layers, accompanied by a slight displacement of the O atoms within the Bi_2O_2 layers (Figure 2a(III,IV)).[13a] Besides, the slight rotation displacement of the oxygen square in the tetragonal Bi_2O_2 layers can simultaneously reduce the crystallographic symmetry from intrinsic D_{4h} to C_{4h},[13b] confirmed by the polarization-dependent high harmonic generations (THG) test.[22] At present, although the ferroelectric transition of Bi_2O_2Se under strain can be regarded as an "interlayer sliding ferroelectric transition" in DFT calculations,[15a,23] its microscopic mechanism has not been elucidated yet.

To shed light on the room-temperature ferroelectricity in CVD-grown Bi_2O_2Se semiconductors, we then conduct the dual AC resonance tracking PFM (DART-PFM, Asylum Research) on Bi_2O_2Se. The sample test is conducted by the switching spectroscopy PFM method using a metal-semiconductor-metal (MSM) structure (Figure S2, Supporting Information), and the detailed information is shown in Figure S3 (Supporting Information). Figure 2b shows the typical "OFF-field" shape obtained from domains reversal in ferroelectric materials, exhibiting a sharp 180° phase reversal of polar domains with a butterfly-shaped amplitude loop at the coercive voltage of $\approx V_{DC} = \pm 5$ V. In general, the "OFF-field" hysteresis loops can exclude the effect of spurious electrostrictive and electrochemical forces that can otherwise also induce piezoresponse feedback that appears similar to ferroelectric ones.[24] Thus, the "OFF-field" loops, which solely record the remnant piezoresponse signal of the ferroelectric-induced electromechanical response,[25] are used to investigate the ferroelectric characteristics. The butterfly loop is relatively offset toward the negative voltage direction, indicating the slight influences from non-ferroelectric artifacts, such as charge injection, which is a common characteristic of ultrathin ferroelectrics.[26] In the "ON-field" piezoresponse hysteresis loops, both the abrupt phase loop and large V-shape amplitude loop with a small butterfly pattern are observed (Figure 2c), demonstrating the coexistence of the ferroelectric and electrostrictive deformation in the presence of the strong unidirectional electric field. A similar four cycles of triangular voltage waves have also been imposed on an ultrathin Bi_2O_2Se flake (≈7.93 nm, 12 layers) both in OFF-field and ON-field states, and a similar switchable polarization is also well observed (Figure S4, Supporting Information). These results verify the OOP ferroelectricity of Bi_2O_2Se and are in good agreement with conventional ferroelectric materials.[27]

Figure 2d presents the topographic image of the corresponding Bi_2O_2Se flake with an ultrathin thickness of 7.3 nm (≈12 layers), and the OOP PFM mappings are shown in Figures 2e (amplitude) and Figure 2f (phase), respectively. According to the OOP PFM mapping of the amplitude, the average vertical piezoelectric deformation ($\overline{\Delta z}$ = 8.8 ± 0.2 pm) versus the original state can be extracted after correcting the resonance-amplified $\overline{\Delta z}$ using the software package of Igor Pro integrated into AR SPM software. According to the equation of $d_{33} = \delta(\overline{\Delta z}) / \delta V_{AC}$, the piezoelectric coefficient (d_{33}) is experimentally calculated to be 4.4 ± 0.1 pm V^{-1}, superior to the most piezoelectric constant of the reported 2D materials thus far. A systematic comparison of the piezoelectric coefficient with other experimentally measured 2D materials is summarized in **Table 1**. We find that the coefficient (d_{33}) of 7.3 nm Bi_2O_2Se is of a similar magnitude to the piezoelectric coefficient of the 4 nm SnS_2 (d_{33}),[30] monolayer 1T-MoS_2 (d_{11}),[31] and WSe_2 (d_{11}),[32] and significantly higher than 5 nm α-In_2Se_3 (d_{33})[29] and 20-nm 2H-$MoTe_2$ (d_{33}).[28] In addition, the piezoelectric effect in Bi_2O_2Se can effectively screen the increased ionized impurity scattering caused by the higher carrier concentration, resulting in the further improvement of its ultrahigh mobility.[33]

© 2023 Wiley-VCH GmbH

15214095, 2023, 12, Downloaded from https://onlinelibrary.wiley.com/doi/10.1002/adma.202210854 by City University Of Hong Kong, Wiley Online Library on [19/04/2023]. See the Terms and Conditions (https://onlinelibrary.wiley.com/terms-and-conditions) on Wiley Online Library for rules of use; OA articles are governed by the applicable Creative Commons License

15214095, 2023, 12, Downloaded from https://onlinelibrary.wiley.com/doi/10.1002/adma.202210854 by City University Of Hong Kong, Wiley Online Library on [19/04/2023]. See the Terms and Conditions (https://onlinelibrary.wiley.com/terms-and-conditions) on Wiley Online Library for rules of use; OA articles are governed by the applicable Creative Commons License

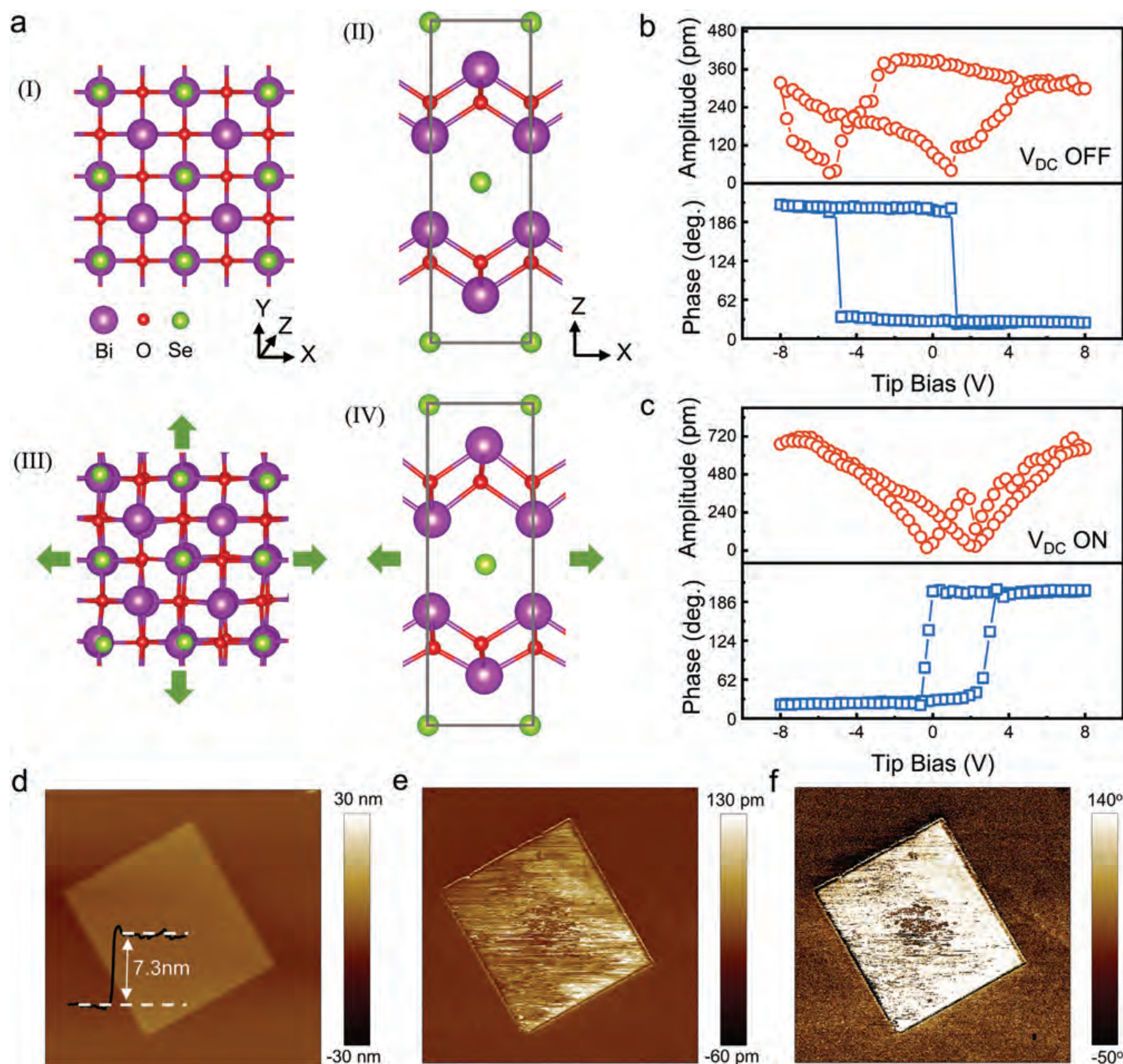

Figure 2. a) Tetragonal unit cell of Bi_2O_2Se from the top view (I) and the side view (II). (III,IV) Tetragonal unit cell of Bi_2O_2Se with spontaneous distortion from the top view (III) and the side view (IV). b,c) Piezoelectric hysteresis loops were conducted by applying DC voltage that sweeps from −8.0 to 8.0 V at 2.0 V AC drive voltage using DART-PFM. Amplitude (upper panel) and phase (lower panel) hysteresis loops with the DC field OFF (b) and the DC field ON (c). d) PFM height, e) PFM phase, and f) PFM amplitude images of a 7.3-nm-thick Bi_2O_2Se on the Au film deposited on a heavily p-doped silicon substrate.

2.3. Switchable Ferroelectric Polarization in Bi_2O_2Se Semiconductors

Further insight into the ferroelectricity of Bi_2O_2Se can be acquired from the calculation of local dipoles in the AIMD simulation at room temperature. **Figure 3**a shows a snapshot of ultrathin Bi_2O_2Se from the ground state MD simulation at room temperature. A spontaneously distorted lattice of Bi_2O_2Se can be observed at room temperature, exhibiting the random orientations and fluctuations of local dipoles at every moment (Figure 3b). The reason is that the energy barrier between the distorted and pristine structure for Bi_2O_2Se is calculated at ≈4.3 meV,[15b] which is much lower than k_BT (k_B is the Boltzmann constant) at room temperature (≈25.9 meV), causing a fluctuating scenery of local dipoles. Compared with the pristine undistorted unit cell, the distances of the Bi-O bonds are shortened from 2.342 Å to 2.2436 Å, 2.242 Å, and 2.274 Å in a typically distorted lattice, simultaneously exhibiting a considerable rotation of O atoms within the Bi_2O_2 layers (Figure 3c). Similarly, slight atomic displacements of Se atoms with regard to Bi atoms are also present in the distorted lattice. The accompanying OOP geometry distortions between the O/Se

 © 2023 Wiley-VCH GmbH

Table 1. Comparison of several 2D materials and their measured piezoelectric constants.

Material	Thickness	Piezoelectric constant	Experimental Value [pm V^{-1}]
2H-$MoTe_2$[28]	20 nm	d_{33}	0.4
α-In_2Se_3[29]	5 nm	d_{33}	≈1.17
SnS_2[30]	4 nm	d_{33}	2.2
1T-MoS_2[31]	monolayer	d_{11}	3.78
WSe_2[32]	monolayer	d_{11}	5.2
3R-like MoS_2/WS_2[27a]	>1.5 nm	d_{33}	2.09
Bi_2O_2Se (this work)	7.3 nm	d_{33}	4.4

and Bi atoms change the size of the unit cell and reduce the space group symmetry of the Bi_2O_2Se lattice, leading to a net OOP ionic polarization in the pristine Bi_2O_2Se lattice.[34] The intriguing ferroelectric order appears with room-temperature stability, as the spontaneous orthorhombic distortion facilitates the formation of spontaneous dipole moments in the ultrathin Bi_2O_2Se lattice.

To probe the origins of the electrically dependent ferroelectricity of the distorted Bi_2O_2Se after AIMD analysis, we thus performed the DFT calculations on the distorted Bi_2O_2Se with symmetry breaking. Figure 3d,e exhibits the OOP electron density redistribution ($\Delta\rho$) of the distorted lattice under the electric field of ±0.1 V $Å^{-1}$, respectively. The related line profiles of the average $\Delta\rho$ along the Z direction under the electric field of +0.1 V $Å^{-1}$ and –0.1 V $Å^{-1}$ are shown in Figure 3f,g, respectively. An opposite charge redistribution under a positive/negative electric field (Figure 3f,g; Figure S5, Supporting Information) explicitly demonstrates that the electric polarization and the polarization direction are switchable. Notably, owing to the electric field, the asymmetry of the OOP electron density redistribution becomes prominent, indicating the broken wave function symmetry, leading to the net ionic polarization. The relationship between the wave function of the occupied states $W_n^{(\lambda)}(r)$ and the electronic contribution to ferroelectric polarization $P_e(\lambda)$ is given by $P_e(\lambda) = -\frac{e}{\Omega}\sum_{n=0}^{M}\int r\,|W_n^{(\lambda)}(r)|^2\,dr$, where e is the charge, Ω is the volume of the unit cell, r is the displacement vector, and $W_n^{(\lambda)}(r)$ is the Wannier wave function of the occupied states.[12,35]

2.4. Interplay Between Ferroelectricity and Semiconducting Characteristics

As shown in **Figure 4**a and Figure S6 (Supporting Information), the back-gated 2D Bi_2O_2Se FET with a high effective oxide thickness (EOT) (270 nm) exhibits excellent electronic transport properties with a clockwise hysteresis. The clockwise hysteresis window, instead of typical ferroelectric-induced counterclockwise ones[36] is observed as swept to a larger V_{GS} (Figure 4b,c). This can be attributed to the insufficient electric field across the Bi_2O_2Se channel, which cannot achieve the ferroelectric polarization in high EOT. The clockwise hysteresis in the 2D layered Bi_2O_2Se FeS-FETs with high EOT is relatively irrelevant to their ferroelectricity. To probe the interplay between ferroelectricity and semiconducting characteristics of Bi_2O_2Se on the device-level operation, we thus fabricate the low-EOT Bi_2O_2Se FETs using 10 nm thick high-κ 10 nm Al_2O_3 as the top-gated dielectric. The device exhibits a typical counterclockwise memory window (MW) (Figure 4d,e; Figure S7, Supporting Information), increasing as swept to the larger V_{GS}. This is because the enhanced polarization intensity and ferroelectric switching appear with the increase of the external electric field in low EOT.[37] A detailed discussion will be made later. Therefore, a large on/off ratio > 10^4 and MW to sweep range (M.W./S.R.) of 47% are obtained at a small V_{GS} of ±5 V (Figure 4f ; Figure S8, Supporting Information). Compared with the ferroelectric/2D material devices reported thus far (Table S1, Supporting Information), 2D layered Bi_2O_2Se ferroelectric semiconductors with switchable polarization exhibit both superior memory performance and excellent electric transport properties in a single material platform, potentially suitable for device simplification and high density integration in von Neumann architecture.[38]

Compared with the traditional ferroelectric field-effect transistors[39] (Figure S9, Supporting Information), both mobile charges (owing to semiconducting characteristics) and polarized bound charges (owing to the ferroelectricity) coexist in the Bi_2O_2Se channel in 2D Bi_2O_2Se FeS-FETs[40] (Figure 4g). To investigate the hysteretic behavior in FeS-FETs, two types of EOT conditions are separately analyzed in this study: low and high EOT. The major difference between a high-EOT device and a low-EOT device is the strength of the electric field across the semiconductor.[41] Figure 4h and Figure S10 exhibit the relative strength of the electric field in high EOT/low EOT under maximum gate voltages by introducing V_{GS}/EOT as a new x-axis, assuming that the electric displacement field is continuous across the dielectric/semiconductor.[42] The maximal relative strength of the electric field (max voltage/EOT) for the high EOT device (270 nm thick SiO_2) is ≈0.29 V nm^{-1}, while for the low-EOT device with (10 nm thick Al_2O_3) is ≈1.16 V nm^{-1}.[41] Due to the insufficient electric field across the channel in high EOT, channel polarization and localized mobile charges distribution cannot be effectively modulated.[43] Therefore, a typical clockwise hysteresis, as widely observed in most n-type FETs,[44] can be observed in 2D Bi_2O_2Se FeS-FETs with high EOT (270 nm thick SiO_2), which is mainly due to the interface trapping and intrinsic defects or traps in semiconductor channels.[45] Thus, in a higher EOT case using 8 nm thick Al_2O_3/270 nm thick SiO_2 as the gate dielectric, a clockwise hysteresis of the 2D Bi_2O_2Se FeS-FETs can be expected to show the typical clockwise hysteresis, which has been verified by our experimental observations (Figure S11, Supporting Information).

Unlike the abovementioned clockwise hysteresis, the counterclockwise hysteresis serves as conclusive proof of ferroelectricity and polarization switching. Based on the related analysis in In_2Se_3 FeS-FETs,[41] a similar simplified model of FeS-FET is introduced. Figure 4i(I) shows the band diagram of the top-gated Bi_2O_2Se FeS-FET with low EOT (Figure 4d; Figure S12, Supporting Information). In this low-EOT condition, the relatively strong electric field across the Al_2O_3 dielectric is sufficiently large that it can penetrate fully into the semiconductor and induce polarization switching in the Bi_2O_2Se channel. When a negative voltage larger than the coercive voltage (V_{C-})

© 2023 Wiley-VCH GmbH

15214095, 2023, 12, Downloaded from https://onlinelibrary.wiley.com/doi/10.1002/adma.202210854 by City University Of Hong Kong, Wiley Online Library on [19/04/2023]. See the Terms and Conditions (https://onlinelibrary.wiley.com/terms-and-conditions) on Wiley Online Library for rules of use; OA articles are governed by the applicable Creative Commons License

15214095, 2023, 12, Downloaded from https://onlinelibrary.wiley.com/doi/10.1002/adma.202210854 by City University Of Hong Kong, Wiley Online Library on [19/04/2023]. See the Terms and Conditions (https://onlinelibrary.wiley.com/terms-and-conditions) on Wiley Online Library for rules of use; OA articles are governed by the applicable Creative Commons License

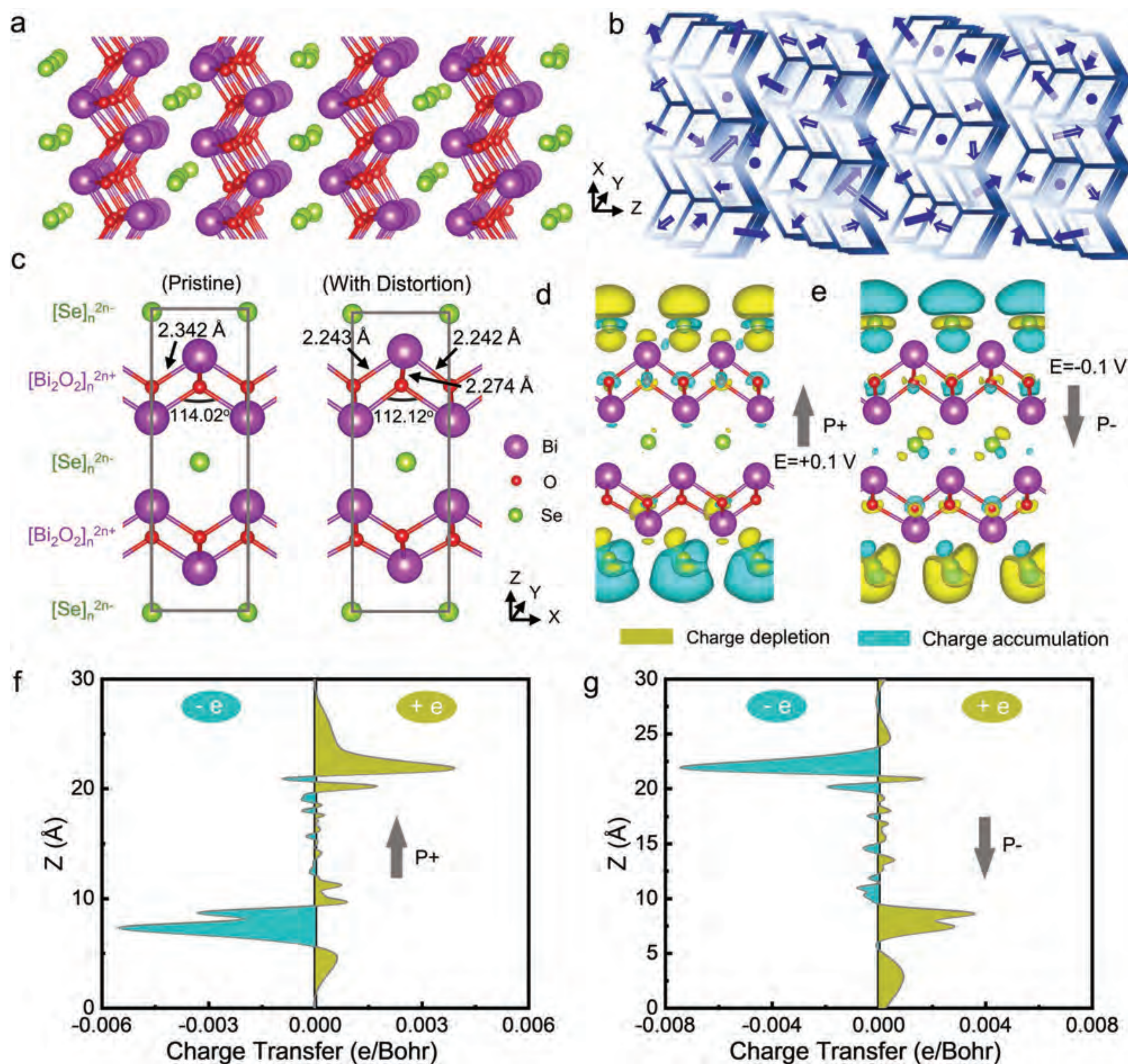

Figure 3. a) Lattice distortion of the one-unit-cell thickness (12.16 Å) of Bi_2O_2Se simulated by the AIMD simulation at room temperature. b) Schematic of the local dipoles with spontaneous distortion calculated as the sum of the product between the displacements and formal charges of Bi/O/Se atoms with reference to the pristine state. c) Comparison of the atomic structure between the pristine and distorted lattice in a unit cell without the external electric field. d,e) Electron density redistribution ($\Delta\rho$) of the distorted lattice under the electric field of ±0.1 V $Å^{-1}$ with an iso-surface value of 3.0×10^{-5} e $bohr^{-3}$, respectively. The baby blue (yellow) color exhibits an electron-rich (deficient) region. The $\Delta\rho$ is denoted as the electron density difference between the electron density (ρ_e) of the Bi_2O_2Se with the electric field and the electron density (ρ_0) of the Bi_2O_2Se without the electric field ($\Delta\rho = \rho_e - \rho_0$). f,g) Line profiles of the average $\Delta\rho$ along the Z-direction under the electric field of +0.1 V $Å^{-1}$ and −0.1 V $Å^{-1}$, respectively. An opposite charge redistribution under lateral sliding of one layer demonstrates that the explicit electric polarization and the polarization direction are switchable.

is applied, the Bi_2O_2Se channel will be fully polarized up. In this case, the mobile charge at the semiconductor/dielectric interface (top surface), which is much easier to control with the gate voltage, is fully depleted under a sufficiently large electric field. Therefore, the FeS-FET exhibits a high resistance state (HRS) of the semiconductor channel. Similarly, the Bi_2O_2Se channel will be fully polarized down when the positive voltage exceeds the coercive voltage (V_{C+}). Due to the complete polarization switching of the channel, electrons can accumulate at the bottom surface resulting in LRS (Figure 4i(II)). Under the reverse V_{GS} sweep, a smaller electric field is required to maintain the same channel carrier density owing to the electron accumulation,[46] leading to a relatively negative shift of the reverse threshold voltage (V_{th1}) with reference to the forward threshold voltage (V_{th0}). As a result, a counterclockwise hysteresis in low EOT can be obtained in a bidirectional sweep

15214095, 2023, 12, Downloaded from https://onlinelibrary.wiley.com/doi/10.1002/adma.202210854 by City University Of Hong Kong, Wiley Online Library on [19/04/2023]. See the Terms and Conditions (https://onlinelibrary.wiley.com/terms-and-conditions) on Wiley Online Library for rules of use; OA articles are governed by the applicable Creative Commons License

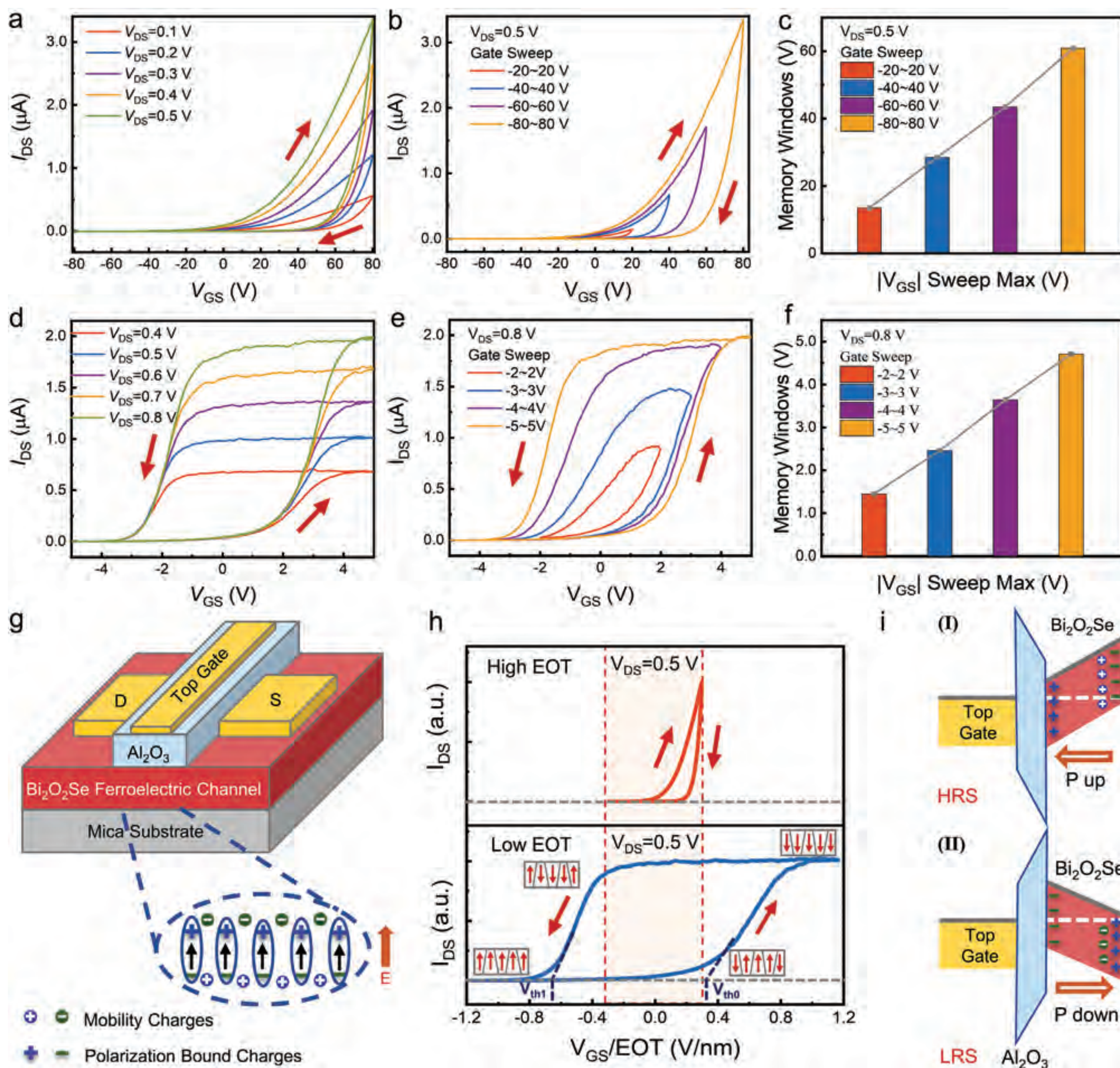

Figure 4. a,b) Transfer characteristics of a back-gated Bi_2O_2Se FET with clockwise hysteresis under different V_{DS} bias (a) and V_{GS} sweep range (b) using 270 nm thick SiO_2 as the dielectric layer. The bidirectional transfer curves are acquired by the same electric field sweeping sequence: −80 V → 80 V → −80 V. c) MWs linearly increase as a function of maximum $|V_{GS}|$. d,e) Transfer characteristics of a top-gated Bi_2O_2Se FeS-FET with counterclockwise hysteresis under different V_{DS} sweep bias (d) and V_{GS} sweep range (e) using 10 nm thick Al_2O_3 as the dielectric layer. The bidirectional transfer curves have the same electric field sweeping sequence: −5 V → 5 V → −5 V. f) MWs linearly increase to 4.7 V under the maximum $|V_{GS}|$ of 5 V. g) Schematic of the top-gated Bi_2O_2Se FeS-FET using low HOT as the dielectric layer. The zoom-in figure shows a polarized upward state, where the positive and negative polarized bound charges are distributed on the top and bottom surfaces, respectively, simultaneously attracting the counterpart negative and positive mobile charges. h) Comparison of hysteretic behaviors in high EOT (clockwise) and low EOT (counterclockwise) at V_{DS} = 0.5 V by introducing V_{GS}/EOT as the new *x*-axis in transfer curves. i) Band diagram of the low-EOT top-gated FeS-FET in full polarization (P) up (I) and P down states (II).

measurement. Notably, the above analysis is a simplified picture that merely considers the band bending induced by polarized bound charges, without considering the band bending resulting from the mobility charges.[47] The theoretical analysis for the clockwise/counterclockwise hysteresis of FeS-FETs matches our experimental observation well with previously reported 2D In_2Se_3 FeS-FETs.[40,41,48]

2.5. Coupling Effect between Photoelectricity and Ferroelectricity

The coupling between ferroelectric and semiconducting properties of Bi_2O_2Se lays the foundation for electrically regulatable optoelectronic devices.[49] **Figure 5**a shows the structure of the FeS-PDs, and its temporal photoresponse with different polarization levels is investigated (Figure 5b). Figure 5c exhibits the

 © 2023 Wiley-VCH GmbH

15214095, 2023, 12, Downloaded from https://onlinelibrary.wiley.com/doi/10.1002/adma.202210854 by City University Of Hong Kong, Wiley Online Library on [19/04/2023]. See the Terms and Conditions (https://onlinelibrary.wiley.com/terms-and-conditions) on Wiley Online Library for rules of use; OA articles are governed by the applicable Creative Commons License

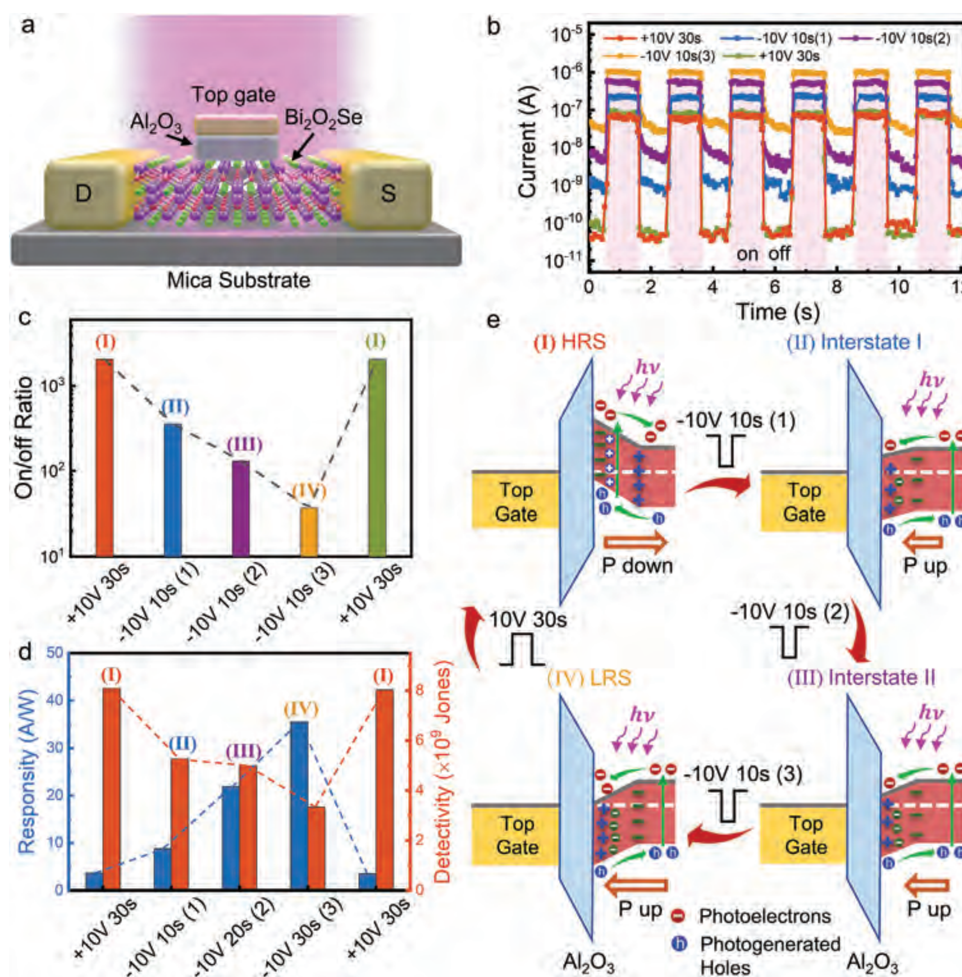

Figure 5. a) Schematic diagram of the top-gated photodetector using the ferroelectric Bi_2O_2Se channel as the photosensitive layer. b) Photoresponse of the FeS-PD device under 405 nm illumination at a power intensity of 1.1184 mW cm^{-2} after withdrawal of distinct gate pulses. c,d) Dependence of the on/off ratio (c) and R and detectivity (d) after withdrawal of distinct gate pulses. e) Band diagrams of the FeS-PD in HRS, Interstate I, Interstate II, and LRS after the withdrawal of different gate pulses, and enhanced separation of the photogenerated electron-hole pairs under 405 nm illumination induced by the remanent polarization, respectively.

different polarization levels of the FeS-PD channel in different bistable channel resistance states: HRS, interstate I, interstate II, and LRS, in which photo- and dark-current can be sequentially regulated by the corresponding gate pulse.[50] At present, photodetectivity is often limited by the low photoresponsivity or a high dark current because of an unavoidable trade-off between photoresponsivity and on/off current ratio under light illumination and dark states.[51] Promisingly, the FeS-PD provides a new avenue for good trade-offs between photoresponsivity and sensitivity since either photodetectivity (D*) or high photoresponsivity (R) can be controllably regulated by a specific gate pulse (Figure 5d). Such a photodetector operation concept based on ferroelectric semiconductors allows the photodetector to have advanced functionality with easy integration and simplified structure, potentially serving the other 2D ferroelectric semiconductors.

A possible photoresponse mechanism of the FeS-PD under each operation is further uncovered based on ferroelectric polarization switching. The orderly ferroelectric polarization can be well maintained after a gate pulse, as electron accumulation in Bi_2O_2Se creates a built-in electric field to consolidate and strengthen the remnant polarization accordingly.[40b] Figure 5e shows the band diagrams of the FeS-PD induced by the remanent polarization and the possible separation of the photogenerated electron-hole pairs under 405 nm illumination. The change of channel resistance can be regarded as a reflection of ferroelectric polarization in Bi_2O_2Se,[52] owing to the coupling of ferroelectricity with semiconducting characteristics. After the withdrawal of the positive pulse (+10 V, 30 s), the energy band bends upward (Figure 5e(I)), resulting in an electron-depleted HRS.[40a,53] As the channel is in HRS, the dark current is sufficiently low (3.2×10^{-11}A), leading to a high on/off ratio of 2.04×10^3. As the negative gate pulse (–10 V, 10 s) is sequentially applied, more ferroelectric domains are orderly polarized up and well maintained.[48,54] The increasingly steeper upward band bending (Interstate I, Interstate II, and LRS) (Figures 5e(II–IV)) leads to a gradually decreased channel resistance, yielding the increased dark current and photocurrent accordingly. However, due to the rapid growth of dark current, the on/off ratio and photodetectivity gradually decrease

© 2023 Wiley-VCH GmbH

ADVANCED MATERIALS
www.advmat.de

while the photoresponsivity increases correspondingly. It is noted that the HRS state can be reproducibly recovered by applying a sufficiently large positive pulse (+10 V, 30 s), owing to the electrically switchable resistance states of the ferroelectric semiconducting photosensitive channel. The above analysis for the FeS-PD matches our experimental observations, providing valuable perspectives on FeS-PDs, which could further explore the fundamental issue and develop high-performance multifunctional optoelectronic devices.

3. Conclusion

To summarize, we investigated the room-temperature OOP ferroelectricity of CVD-grown Bi_2O_2Se with a thickness of 7.3 nm (≈12 layers). The electrically ferroelectric polarization switching of Bi_2O_2Se is directly probed by DART-PFM, and its ferroelectric origin is uncovered by detailed AIMD simulation and DFT calculation. In addition, the piezoelectric coefficient of Bi_2O_2Se is experimentally measured (d_{33} = 4.4 ± 0.1 pm V^{-1}) superior to the most piezoelectric constant of the reported 2D materials thus far. Specifically, the interplay between ferroelectricity and semiconducting characteristics of Bi_2O_2Se on the device-level operation is explored, exhibiting a large M.W./S.R. of 47% and an on/off ratio > 10^4 at V_{GS} = ±5 V. Also, the trade-off between R and sensitivity for FeS-PDs is uncovered based on the electrically switchable polarization in semiconducting Bi_2O_2Se channels. Overall, switchable ferroelectric polarization in Bi_2O_2Se semiconductors potentially provides a powerful material platform for merging sensing, logic, and memory functions into a single material system, potentially overcoming the bottlenecks of device simplification and high-density integration in von Neumann architecture.

4. Experimental Section

Methods: Bi_2O_2Se flakes were grown by the CVD method.[16] Bi_2Se_3 (Aldrich, 99.99%) and Bi_2O_3 (Thermo Fisher, 98%) powder were placed on both sides of a 5 cm quartz boat. The quartz boat of the Bi_2O_3 side was put in the center of the heating zone, and the mica substrate was placed downstream, 10–14 cm away from the center. The furnace was heated to 635–650 °C with a ramping time of 10 min and a holding time of 10–25 min under ≈120 torr. Ahead of the heating process, the furnace tube was flushed with high-purity argon gas to exhaust the atmospheric moisture and oxygen thoroughly. After high-temperature deposition, the furnace was naturally cooled to room temperature.

Device Fabrication: For the back-gated FETs, the as-grown Bi_2O_2Se flakes were detached from mica and transferred to the desired dielectric substrate by a PMMA-assisted wet transfer method (Figure S13, Supporting Information). The Au electrodes were patterned by electron-beam lithography and thermally evaporated with a thickness of 40 nm. For the top-gated FeS-FETs, the Au electrodes were patterned by a standard photolithography process and thermally evaporated with a thickness of 40 nm.

Characterization: The topological morphologies of the materials were characterized by optical and AFMs (Dimension Icon, Bruker), respectively. The ferroelectric polarization flip was tested by the DART-PFM (Asylum Research) using a MSM structure. Raman spectra were collected by a confocal microscope spectrometer (Alpha 300R, WITec). The corresponding crystal structures and crystallinity were characterized by analyzing the XRD pattern and imaging with HRTEM (Tecnai G2 F30, FEI). The electronic and photodetection performance was tested by a semiconductor analyzer (Agilent 4155C) and probe station under different laser sources (405 nm), whose power intensity was calibrated by a power meter (PM400, Thorlabs).

Supporting Information

Supporting Information is available from the Wiley Online Library or from the author.

Acknowledgements

W.W.J. and M.Y. contributed equally to this work. This research was financially supported by a fellowship award from the Research Grants Council of the Hong Kong Special Administrative Region, China (CityU RFS2021-1S04), Shenzhen Municipality Science and Technology Innovation Commission (grant no. SGDX2020110309300402; "Modulation and Detection of Terahertz Waves based on Semi-Metallic 2D Materials", CityU), and Foshan Innovative and Entrepreneurial Research Team Program (No. 2018IT100031).

Conflict of Interest

The authors declare no conflict of interest.

Data Availability Statement

The data that support the findings of this study are available from the corresponding author upon reasonable request.

Keywords

Bi_2O_2Se, ferroelectric semiconductors, von Neumann architecture

Received: November 21, 2022
Revised: January 3, 2023
Published online: February 8, 2023

[1] Z. Guan, H. Hu, X. W. Shen, P. H. Xiang, N. Zhong, J. H. Chu, C. G. Duan, *Adv. Electron. Mater.* **2020**, *6*, 1900818.
[2] N. A. Spaldin, *Science* **2004**, *304*, 1606.
[3] H. von Seggern, S. Fedosov, *IEEE. Trans. Dielectr. Electr. Insul.* **2000**, *7*, 543.
[4] a) F. Xue, W. Hu, K.-C. Lee, L.-S. Lu, J. Zhang, H.-L. Tang, A. Han, W.-T. Hsu, S. Tu, W.-H. Chang, C.-H. Lein, Z. Zhang, L.-J. Li, X. Zhang, *Adv. Funct. Mater.* **2018**, *28*, 1803738; b) Y. Nezu, Y.-Q. Zhang, C. L. Chen, Y. Ikuhara, H. Ohta, *J. Appl. Phys.* **2017**, *122*, 135305.
[5] E. Yurchuk, J. Muller, S. Muller, J. Paul, M. Pesic, R. van Bentum, U. Schroeder, T. Mikolajick, *IEEE. Trans. Electron Devices* **2016**, *63*, 3501.
[6] Y.-T. Huang, N.-K. Chen, Z.-Z. Li, X.-P. Wang, H.-B. Sun, S. Zhang, X.-B. Li, *InfoMat* **2022**, *4*, 12341.
[7] S. Wan, Y. Li, W. Li, X. Mao, W. Zhu, H. Zeng, *Nanoscale* **2018**, *10*, 14885.
[8] a) M. Osada, T. Sasaki, *APL Mater.* **2019**, *7*, 120902; b) S. G. Yuan, X. Luo, H. L. Chan, C. Xiao, Y. Dai, M. Xie, J. Hao, *Nat. Commun.* **2019**, *10*, 1775.

© 2023 Wiley-VCH GmbH

15214095, 2023, 12, Downloaded from https://onlinelibrary.wiley.com/doi/10.1002/adma.202210854 by City University Of Hong Kong, Wiley Online Library on [19/04/2023]. See the Terms and Conditions (https://onlinelibrary.wiley.com/terms-and-conditions) on Wiley Online Library for rules of use; OA articles are governed by the applicable Creative Commons License

[9] Z.-D. Luo, M.-M. Yang, Y. Liu, M. Alexe, *Adv. Mater.* **2021**, *33*, 2005620.
[10] W. J. Ding, J. B. Zhu, Z. Wang, Y. F. Gao, D. Xiao, Y. Gu, Z. Y. Zhang, W. G. Zhu, *Nat. Commun.* **2017**, *8*, 14956.
[11] Z. Y. Fei, W. J. Zhao, T. A. Palomaki, B. S. Sun, M. K. Miller, Z. Y. Zhao, J. Q. Yan, X. D. Xu, D. H. Cobden, *Nature* **2018**, *560*, 336.
[12] Y. Bao, P. Song, Y. P. Liu, Z. H. Chen, M. L. Zhu, I. Abdelwahab, J. Su, W. Fu, X. Chi, W. Yu, W. Liu, X. X. Zhao, Q. H. Xu, M. Yang, K. P. Loh, *Nano Lett.* **2019**, *19*, 5109.
[13] a) M. H. Wu, X. C. Zeng, *Nano Lett.* **2017**, *17*, 6309; b) T. Ghosh, M. Samanta, A. Vasdev, K. Dolui, J. Ghatak, T. Das, G. Sheet, K. Biswas, *Nano Lett.* **2019**, *19*, 5703.
[14] a) J. X. Wu, C. G. Qiu, H. X. Fu, S. L. Chen, C. C. Zhang, Z. P. Dou, C. W. Tan, T. Tu, T. R. Li, Y. C. Zhang, Z. Y. Zhang, L. M. Peng, P. Gao, B. H. Yan, H. L. Peng, *Nano Lett.* **2019**, *19*, 197; b) C. Chen, M. X. Wang, J. X. Wu, H. X. Fu, H. F. Yang, Z. Tian, T. Tu, H. Peng, Y. Sun, X. Xu, J. Jiang, N. B. M. Schroter, Y. W. Li, D. Pei, S. Liu, S. A. Ekahana, H. T. Yuan, J. M. Xue, G. Li, J. F. Jia, Z. K. Liu, B. H. Yan, H. L. Peng, Y. L. Chen, *Sci. Adv.* **2018**, *4*, 8355.
[15] a) Z. Y. Zhu, X. P. Yao, S. Zhao, X. Lin, W. B. Li, *J. Am. Chem. Soc.* **2022**, *144*, 4541; b) F. Wang, W. Chu, L. Huber, T. Tu, Y. Dai, J. Wang, H. Peng, J. Zhao, X.-Y. Zhu, *Proc. Natl. Acad. Sci. U. S. A.* **2022**, *119*, 2122436119; c) Y. Liang, X. Zhou, W. Li, H. Peng, *APL Mater.* **2021**, *9*, 060905.
[16] W. J. Wang, Y. Meng, W. Wang, Z. M. Zhang, P. S. Xie, Z. X. Lai, X. M. Bu, Y. Z. Li, C. T. Liu, Z. B. Yang, S. Yip, J. C. Ho, *Adv. Funct. Mater.* **2022**, *32*, 2203003.
[17] J. X. Wu, H. T. Yuan, M. M. Meng, C. Chen, Y. Sun, Z. Y. Chen, W. H. Dang, C. W. Tan, Y. J. Liu, J. B. Yin, Y. B. Zhou, S. Y. Huang, H. Q. Xu, Y. Cui, H. Y. Hwang, Z. F. Liu, Y. L. Chen, B. H. Yan, H. L. Peng, *Nat. Nanotechnol.* **2017**, *12*, 530.
[18] W. J. Chen, U. Khan, S. M. Feng, B. F. Ding, X. M. Xu, B. L. Liu, *Adv. Funct. Mater.* **2020**, *30*, 2004960.
[19] P. L. Wang, T. Kolodiazhnyi, J. Yao, Y. Mozharivskyj, *J. Am. Chem. Soc.* **2012**, *134*, 1426.
[20] Q. Fu, C. Zhu, X. Zhao, X. Wang, A. Chaturvedi, C. Zhu, X. Wang, Q. Zeng, J. Zhou, F. Liu, B. K. Tay, H. Zhang, S. J. Pennycook, Z. Liu, *Adv. Mater.* **2019**, *31*, 1804945.
[21] F. Wang, Y. Fu, M. E. Ziffer, Y. Dai, S. F. Maehrlein, X.-Y. Zhu, *J. Am. Chem. Soc.* **2020**, *143*, 5.
[22] J. Liang, T. Tu, G. Chen, Y. Sun, R. Qiao, H. Ma, W. Yu, X. Zhou, C. Ma, P. Gao, H. Peng, K. Liu, D. Yu, *Adv. Mater.* **2020**, *32*, 2002831.
[23] Y. Guo, Y. Song, M. Yang, Z. Xu, H. Xie, H. Li, Z. Li, H. Liang, S. Ruan, Y.-J. Zeng, *J. Mater. Chem. C* **2020**, *8*, 13226.
[24] L. Keeney, R. J. Smith, M. Palizdar, M. Schmidt, A. J. Bell, J. N. Coleman, R. W. Whatmore, *Adv. Electron. Mater.* **2020**, *6*, 1901264.
[25] H. Qiao, O. Kwon, Y. Kim, *Appl. Phys. Lett.* **2020**, *116*, 172901.
[26] S. S. Cheema, D. Kwon, N. Shanker, R. dos Reis, S. L. Hsu, J. Xiao, H. G. Zhang, R. Wagner, A. Datar, M. R. McCarter, C. R. Serrao, A. K. Yadav, G. Karbasian, C. H. Hsu, A. J. Tan, L.-C. Wang, V. Thakare, X. Zhang, A. Mehta, E. Karapetrova, R. V. Chopdekar, P. Shafer, E. Arenholz, C. M. Hu, R. Proksch, R. Ramesh, J. Ciston, S. Salahuddin, *Nature* **2020**, *580*, 478.
[27] a) L. Rogee, L. Wang, Y. Zhang, S. H. Cai, P. Wang, M. Chhowalla, W. Ji, S. P. Lau, *Science* **2022**, *376*, 973; b) N. R. Alluri, N. P. M. J. Raj, G. Khandelwal, S. J. Kim, *Nano Energy* **2021**, *88*, 106231.
[28] S. Kang, S. Kim, S. Jeon, W.-S. Jang, D. Seol, Y.-M. Kim, J. Lee, H. Yang, Y. Kim, *Nano Energy* **2019**, *58*, 57.
[29] S. Mukherjee, E. Koren, *Isr. J. Chem.* **2022**, *62*, 202100112.
[30] Y. Wang, L.-M. Vu, T. Lu, C. Xu, Y. Liu, J. Z. Ou, Y. Li, *ACS Appl. Mater. Interfaces* **2020**, *12*, 51662.
[31] S. K. Kim, R. Bhatia, T.-H. Kim, D. Seol, J. H. Kim, H. Kim, W. Seung, Y. Kim, Y. H. Lee, S.-W. Kim, *Nano Energy* **2016**, *22*, 483.
[32] E. N. Esfahani, T. Li, B. Huang, X. Xu, J. Li, *Nano Energy* **2018**, *52*, 117.
[33] a) F. Yang, J. Wu, A. Suwardi, Y. S. Zhao, B. Y. Liang, J. Jiang, J. W. Xu, D. Z. Chi, K. Hippalgaonkar, J. P. Lu, Z. H. Ni, *Adv. Mater.* **2021**, *33*, 2004786; b) N. Maeda, T. Saitoh, K. Tsubaki, T. Nishida, N. Kobayashi, *Jpn . J. Appl. Phys.* **1999**, *38*, L799.
[34] R. Fei, W. Kang, L. Yang, *Phys. Rev. Lett.* **2016**, *117*, 097601.
[35] R. D. Kingsmith, D. Vanderbilt, *Phys. Rev. B* **1993**, *47*, 1651.
[36] a) M. Si, A. K. Saha, S. Gao, G. Qiu, J. Qin, Y. Duan, J. Jian, C. Niu, H. Wang, W. Wu, S. K. Gupta, P. D. Ye, *Nat. Electron.* **2019**, *2*, 580; b) M. Si, P.-Y. Liao, G. Qiu, Y. Duan, P. D. Ye, *ACS Nano* **2018**, *12*, 6700; c) W. Huang, F. Wang, L. Yin, R. Cheng, Z. Wang, M. G. Sendeku, J. Wang, N. Li, Y. Yao, J. He, *Adv. Mater.* **2020**, *32*, 1908040.
[37] P. Gao, J. Britson, J. R. Jokisaari, C. T. Nelson, S. H. Baek, Y. R. Wang, C. B. Eom, L. Q. Chen, X. Q. Pan, *Nat. Commun.* **2013**, *4*, 2791.
[38] M. S. Ram, K.-M. Persson, A. Irish, A. Jönsson, R. Timm, L.-E. Wernersson, *Nat. Electron.* **2021**, *4*, 914.
[39] A. I. Khan, A. Keshavarzi, S. Datta, *Nat. Electron.* **2020**, *3*, 588.
[40] a) P. Singh, S. Baek, H. H. Yoo, J. Niu, J.-H. Park, S. Lee, *ACS Nano* **2022**, *16*, 5418; b) S. Wang, L. Liu, L. R. Gan, H. W. Chen, X. Hou, Y. Ding, S. L. Ma, D. W. Zhang, P. Zhou, *Nat. Commun.* **2021**, *12*, 53.
[41] M. Si, A. K. Saha, S. Gao, G. Qiu, J. Qin, Y. Duan, J. Jian, C. Niu, H. Wang, W. Wu, S. K. Gupta, P. D. D. Ye, *Nat. Electron.* **2019**, *2*, 580.
[42] W. Li, D. Jena, H. G. Xing, *Semicond. Semimetals* **2021**, *107*, 23.
[43] K. Liu, B. Dang, T. Zhang, Z. Yang, L. Bao, L. Xu, C. Cheng, R. Huang, Y. Yang, *Adv. Mater.* **2022**, *34*, 2108826.
[44] a) Y. X. Li, R. R. Liang, J. B. Wang, C. S. Jiang, B. K. Xiong, H. F. Liu, Z. B. Wang, X. F. Wang, Y. Pang, H. Tian, Y. Yang, T. L. Ren, *IEEE Electron. Device Lett.* **2019**, *40*, 826; b) W. Hou, A. Azizimanesh, A. Sewaket, T. Pena, C. Watson, M. Liu, H. Askari, S. M. Wu, *Nat. Nanotechnol.* **2019**, *14*, 668; c) M. Si, Y. Luo, W. Chung, H. Bae, D. Zheng, J. Li, J. Qin, G. Qiu, S. Yu, P. D. Ye, *IEEE Int. Electron Devices Meet.* **2019**, 130.
[45] a) K. Choi, S. R. A. Raza, H. S. Lee, P. J. Jeon, A. Pezeshki, S.-W. Min, J. S. Kim, W. Yoon, S.-Y. Ju, K. Lee, S. Im, *Nanoscale* **2015**, *7*, 5617; b) Y. F. Xia, G. He, W. H. Wang, Q. Gao, Y. M. Liu, *IEEE Trans. Electron Devices* **2021**, *68*, 2522.
[46] Z. Ye, Y. G. Yuan, H. Xu, Y. Liu, J. K. Luo, M. Wong, *IEEE Trans. Electron Devices* **2017**, *64*, 438.
[47] J. Robertson, R. M. Wallace, *Mater. Sci. Eng., R* **2015**, *88*, 1.
[48] X. W. Wang, C. Zhu, Y. Deng, R. H. Duan, J. Q. Chen, Q. S. Zeng, J. D. Zhou, Q. D. Fu, L. You, S. Liu, J. H. Edgar, P. Yu, Z. Liu, *Nat. Commun.* **2021**, 12, 1.
[49] D. Dutta, S. Mukherjee, M. Uzhansky, E. Koren, *npj 2D Mater. Appl.* **2021**, *5*, 81.
[50] W. H. Huang, F. Wang, L. Yin, R. Q. Cheng, Z. X. Wang, M. G. Sendeku, J. J. Wang, N. N. Li, Y. Y. Yao, J. He, *Adv. Mater.* **2020**, *32*, 1908040
[51] a) Q. A. Vu, J. H. Lee, V. L. Nguyen, Y. S. Shin, S. C. Lim, K. Lee, J. Heo, S. Park, K. Kim, Y. H. Lee, W. J. Yu, *Nano Lett.* **2017**, *17*, 453; b) Z. T. Luo, M. M. Yang, D. S. Wu, Z. H. Huang, W. Gao, M. L. Zhang, Y. C. Zhou, Y. Zhao, Z. Q. Zheng, J. B. Li, *Small Methods* **2022**, *6*, 2200583; c) H. Y. Wang, Z. X. Li, D. Y. Li, X. Xu, P. Chen, L. J. Pi, X. Zhou, T. Y. Zhai, *Adv. Funct. Mater.* **2021**, *31*, 2103106.
[52] S. Baek, H. H. Yoo, J. H. Ju, P. Sriboriboon, P. Singh, J. Niu, J. H. Park, C. Shin, Y. Kim, S. Lee, *Adv. Sci.* **2022**, *9*, 2200566.
[53] L. Wang, X. Wang, Y. Zhang, R. Li, T. Ma, K. Leng, Z. Chen, I. Abdelwahab, K. P. Loh, *Adv. Funct. Mater.* **2020**, *30*, 2004609.
[54] Y. B. Sun, S. Y. Wang, X. Z. Chen, Z. H. Zhang, P. Zhou, *Adv. Intell. Syst.* **2022**, *4*, 2100198.

© 2023 Wiley-VCH GmbH

15214095, 2023, 12, Downloaded from https://onlinelibrary.wiley.com/doi/10.1002/adma.202210854 by City University Of Hong Kong, Wiley Online Library on [19/04/2023]. See the Terms and Conditions (https://onlinelibrary.wiley.com/terms-and-conditions) on Wiley Online Library for rules of use; OA articles are governed by the applicable Creative Commons License